Computational Materials Science 248 (2025) 113587

Contents lists available at ScienceDirect

Computational Materials Science

journal homepage: www.elsevier.com/locate/commatsci

Full length article

Chemical short-range order and its influence on selected properties of non-dilute random alloys

Subah Mubassira [a], Mahshad Fani [a], Anshu Raj [a], Cliff Hirt [a], Richard S. Brinlee [a], Amin Poozesh [a], Wu-Rong Jian [b], Saeed Zare Chavoshi [c], Chanho Lee [d], Shuozhi Xu [a,*]

[a] School of Aerospace and Mechanical Engineering, University of Oklahoma, Norman, OK, 73019-0390, United States
[b] Department of Mechanical Engineering, Stanford University, Stanford, CA, 94305, United States
[c] Independent Researcher, London, United Kingdom
[d] Department of Materials and Mechanical Engineering, Auburn University, Auburn, AL, 36849-5337, United States

ARTICLE INFO

Dataset link: https://github.com/shuozhixu/CMS-EAM_2025, https://github.com/shuozhixu/CMS-MEAM_2025, https://github.com/shuozhixu/CMS-MTP_2025

Keywords:
Chemical short-range order
Non-dilute random alloys
Lattice distortion
Unstable stacking fault energy
Melting point

ABSTRACT

In recent years, non-dilute random alloys (NDRAs) have been gaining interest as promising materials for high-temperature structural applications due to their unique ability to form solid solution phases that portray exceptional mechanical properties and resilience under extreme conditions. This study deals with the effects of chemical short-range order (CSRO) on selected material properties including lattice parameter, lattice distortion (LD), unstable stacking fault energy (USFE), and melting point (MP). The main body of this study is on 21 ternary alloys, where the interatomic interactions are described by an embedded-atom method potential. Our results demonstrate that random structures generally exhibit larger lattice parameters and greater LD compared to CSRO structures, while CSRO structures possess higher USFEs and MPs. Furthermore, there is no discernible pattern in the segregation of the same and different atom pairs in the NDRAs, as revealed by the notably varying local ordering or segregation for most of them. Last, the effects of interatomic potential and the number of constituent elements are studied using other interatomic potentials and/or non-ternary systems, suggesting that our finding is consistent across different potentials/alloys.

1. Introduction

The conventional approach to alloy design has largely centered on a principal metallic element serving as the matrix, supplemented by small quantities of additional elements (solutes) aimed at improving characteristics including strength, corrosion resistance, and ductility. These dilute alloys have predominantly focused on the peripheries of multi-component phase diagrams, thereby neglecting the possible interactions among various principal elements [1]. Properties of these alloys are primarily governed by the base metal, with solute elements present in minimal concentrations, usually below 10% [2]. Non-dilute random alloys (NDRAs) are distinguished by having two or more dominant constituents in near equal molar fractions, leading to property features that cannot be directly derived from the pure elements [3]. A good example of NDRAs is multi-principal element alloys (MPEAs), which are composed of three or more constituents in equimolar or near equimolar ratios. The complex interactions among constituents in MPEAs result in improved structural and functional properties which motivated research on alloy design into the central regions of multi-component phase diagrams [4]. Similar to MPEAs, NDRAs can form stable solid solutions on simple lattice structures such as face-centered cubic (FCC), body-centered cubic (BCC), or hexagonal close-packed (HCP) lattices [5–7]. These alloys derive their properties from balanced contributions across all constituent elements, leading to atomic-scale fluctuations including chemical short-range order (CSRO) and lattice distortion (LD). This unique structure imparts NDRAs with exceptional strength, ductility, and resistance to corrosion, irradiation, fatigue, and creep [8,9]. While early studies predominantly focused on FCC-structured NDRAs [10–15], recent research has increasingly highlighted the fascinating properties of BCC NDRAs. Significant advancements have been made in developing refractory MPEAs, particularly those containing elements such as Mo, Nb, Re, Ta, and W [16–18]. Alloys like MoNbTi [19]and NbTiZr [20] exhibit impressive mechanical properties, with compressive yield strengths of 1100 MPa and 975 MPa, respectively, at room temperature. Moreover, these alloys maintain significant strength at elevated temperatures, outperforming pure refractory metals like Mo and Nb [7,18–21].

Although NDRAs are usually considered nominally random alloys, several experimental results, mainly obtained from transmission electron microscopy, have shown that CSRO may develop after prolonged annealing at lower temperatures [22]. CSRO in MPEAs has been

* Corresponding author.
E-mail address: shuozhixu@ou.edu (S. Xu).

https://doi.org/10.1016/j.commatsci.2024.113587
Received 5 November 2024; Received in revised form 26 November 2024; Accepted 29 November 2024

defined as the thermodynamic preferential clustering of one or more atomic species within a few nearest neighbor shells, different from a completely random atomic structure [22–24]. Such ordering introduces localized domains where the formation of specific element pairs or clusters becomes more probable, therefore providing variability in atomic environments across the alloy. More recently, substantial levels of CSRO have been demonstrated in both FCC MPEAs, including CoCrNi [22,25,26] and CoNiV [23], and BCC MPEAs, such as HfNbTiZr [27]. Calculations supporting CSRO in MPEAs have been conducted using density functional theory (DFT) and hybrid Monte Carlo (MC)/molecular dynamics (MD) simulations, with the annealing temperature employed to control the degree and intensity of CSRO [28–36].

Molecular static (MS) simulations indicate that CSRO significantly influences fundamental parameters, including the lattice parameter, elastic constants, and generalized stacking fault energies (GSFEs) [10,37]. Ding et al. [26] performed DFT calculations to investigate the influence of CSRO in CoCrNi MPEA on GSFE, revealing a monotonic increase in GSFE with a higher degree of CSRO. Li et al. [10] employed atomistic simulations to examine the impact of CSRO on dislocation motion in CoCrNi MPEA. They discovered that regions exhibiting high CSRO could serve as effective impediments to dislocation movement, hence augmenting the stress necessary for slip and consequently raising the strength of the alloy. CSRO is also associated with modifications in hardness and the formation of stacking faults, which directly influence ductility and toughness [22]. Jian et al. [34] derived that the localization of LD in CoCrNi MPEA reduces the effective nucleation area for amorphous clusters as the melting starts, which corresponds to a reduction of free energy and therefore to an increase of the melting point (MP) of the CSRO MPEA compared with its random counterpart. In BCC MoNbTaW MPEA, DFT calculations have demonstrated that CSRO contributes to the stabilization of dislocation core configurations, thereby minimizing spatial fluctuations in core energies and enhancing high-temperature strength [36]. Taken together, MPEAs can be designed to achieve desired properties by tuning CSRO through appropriate alloy composition and processing conditions, further enhancing their suitability for demanding structural applications.

Despite a large volume of studies on CSRO, some knowledge gaps exist. Most of the previous studies on CSRO were rather restricted in terms of the number of alloys in a single study, i.e., usually one or two MPEAs at a time. In addition, findings were often disparate due to differences in methods, conditions, and approaches employed in the studies, which did not easily allow for drawing consistent conclusions. In this study, we aim to provide a comprehensive understanding by conducting a systematic investigation across a broad range of alloys to investigate the effects of CSRO on some important mechanical and thermal parameters of NDRAs, including lattice parameter, LD, USFE, and MP. We focus on a set of 21 ternary NDRAs — CoCrNi, HfTiZr, HfNbTa, HfNbTi, HfTaTi, MoNbTa, MoNbTi, MoNbV, MoNbW, MoTaTi, MoTaV, MoTaW, MoVW, NbTaTi, NbTaV, NbTaW, NbTiV, NbTiZr, NbVW, TaTiZr, and TaVW — each comprising three elements in equal molar ratios. The first and second alloys have an FCC and an HCP lattice, respectively, while all other alloys are BCC. Our choice of compositions allows for a comprehensive analysis of the effects of CSRO across different configurations. We derive the effect of CSRO by comparing properties of these alloys influenced by CSRO with those of random atomic configurations within the same systems. We first quantify how segregation or local ordering of the atomic pairs varies across these NDRAs. Then we analyze how the CSRO influences properties such as lattice parameter, LD, USFE, and MP. Moreover, we examine if our results are dependent on the interatomic potential or the number of constituent elements. For this purpose, we will employ two additional interatomic potentials and study three binaries (NbTa, NbTi, NbV), one quinary (NbTaTiV), and one quaternary (NbTaTiVZr). These studies are aimed at providing a comprehensive understanding of how CSRO influences selected properties of NDRAs and thus provide a useful guide for the optimization of high-performance alloys towards future applications.

2. Methods and materials

Atomistic simulations are carried out by LAMMPS [38]. The interatomic interactions in NDRAs are modeled with the embedded-atom method (EAM) potential [39], unless stated otherwise. The EAM potential for the CoCrNi system is developed by Li et al. [10]. For all other alloys, the eight elemental potentials are: Hf [40], Mo [41], Nb [42], Ta [41], Ti [41], V [43], W [41], Zr [41]. Cross interactions between different elements are based on the formulation of Zhou et al. [41].

2.1. CSRO formation

To understand the effect of CSRO on material properties, we first generate both random and CSRO NDRA structures. Based on the random structure, we implement a hybrid MD/MC simulation for CSRO formation in an isothermal–isobaric (NPT) ensemble at 300 K, which is performed until the energy of the system converges to a constant [10,14,44–46]. The Warren-Cowley (WC) parameters are determined using

$$\alpha_{ij}^{n} = \frac{p_{ij}^{n} - c_j}{\delta_{ij} - c_j} \tag{1}$$

where n signifies the nth-nearest-neighbor shell of the central atom of type-i, p_{ij}^{n} denotes the probability of locating a j-type atom around an atom of type i within the nth shell, c_j is the concentration of j-type atom, and δ_{ij} is the Kronecker delta function [47,48]. In a fully random structure, the value α_{ij}^{n} is expected to be close to zero, whereas a higher magnitude value of α_{ij}^{n} indicates a greater degree of CSRO. A positive α_{ij}^{n} value suggests the segregation of the same species ($i = j$). In contrast, the negative value of α_{ij}^{n} corresponds to the local ordering of the different species ($i \neq j$). In this paper, only the 1st nearest neighbor distance is considered, i.e., $n = 1$.

The simulation cell sizes for different alloys are similar. First, all BCC alloys have the same number of atoms of 38,640, only differing in lattice parameter. Take MoNbTa as an example, the three edge lengths of the cell are 7.9 nm, 12.9 nm, and 6.4 nm, respectively. The cell for HCP HfTiZr has 29,952 atoms, while that for FCC CoCrNi has 54,000 atoms. The effects of cell size on potential energy convergence and WC parameters are shown in Figs. A.12 and A.13, respectively.

2.2. Lattice parameter

We employ the relaxation method to calculate the lattice parameter of the NDRAs. In this method, a unit cell with a predefined lattice parameter 3.3 Å is generated. Subsequently, the system is relaxed such that the three normal stress components are zero. Based on the resultant relaxed unit cell's volume, the lattice parameter, a_0, is calculated.

2.3. LD

In the literature, there are at least four ways to quantify the average LD in atomistic simulations [49]. The first one is based on the difference in the lattice parameters among all constituent elements [50]; the second one is based on the "local lattice strain" [51]; the third one uses the full width at half maximum (FWHM) of the radial distribution function [32]; the last one is the root mean squared atomic displacement (RMSAD), defined as the average displacement of relaxed atoms from their ideal positions in the undistorted crystal lattice [52,53]. All four ways take into account the chemical compositions and their nominal molar ratios, while the last three additionally consider the distribution of atoms. As a result, the first method yields the same LD for two atomistic structures with the same composition but differing CSROs. Recently, Jian et al. [32] and Chen et al. [23] studied CoCrNi and NbTiZr respectively, and observed that the FWHM in the CSRO structures is smaller than that in their random counterparts. In contrast, Wang et al. [54] showed that in five out of six BCC NDRAs, RMSAD is larger in CSRO structures than in random ones. These findings suggest that the impact of CSRO on LD may vary depending on the definition of LD. Our objective is to systematically address this discrepancy by comparing both LD definitions.

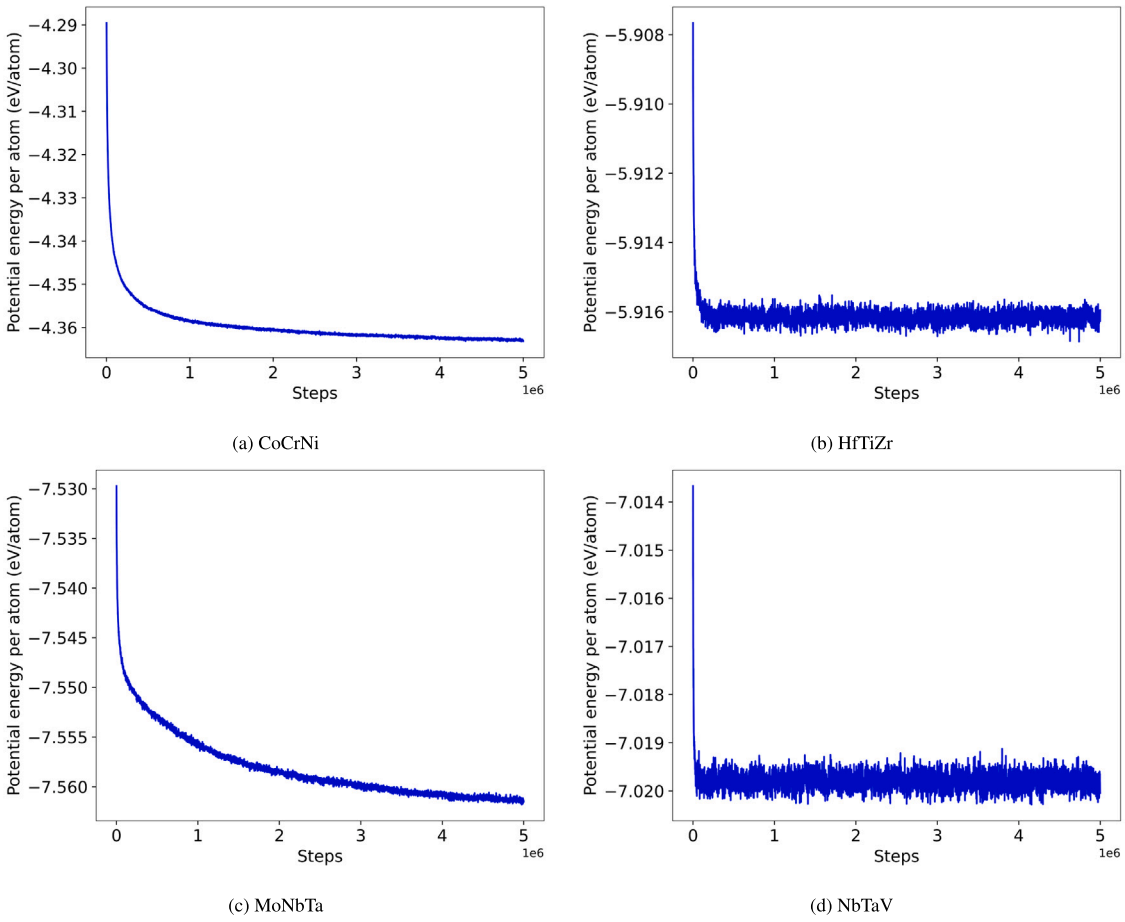

Fig. 1. Convergence of potential energy per atom as a function of simulation steps for the CSRO structures of four NDRAs: (a) CoCrNi, (b) HfTiZr, (c) MoNbTa, and (d) NbTaV, based on the EAM potential.

2.4. USFE

In FCC crystals, USFE is the smaller local maximum on the GSFE curve along the ⟨112⟩ direction on the {111} plane. Similarly, on the basal plane in HCP crystals, USFE is the smaller local maximum on the GSFE curve along the ⟨1100⟩ direction on the {0001} basal plane. In BCC crystals, USFE is the maximum value on the GSFE curve along the ⟨111⟩ direction on the {110} plane. The GSFE quantifies the energy required to shear a crystal lattice along a specific plane and provides valuable information on mechanical properties such as strength. In this study, to create GSFE curves, we shift the top half of the samples along a specified direction within a specific plane. The computations include displacements across a single periodic distance, which is equivalent to the Burgers vector magnitude for a full dislocation, b. In the same alloy system, the value of USFE γ_{gsf} varies between different parallel slip planes because the latter have varying local atomic environments [26,55–57]. Therefore, GSFE curves are computed on 20 different planes in each NDRA for reliable consistency [58].

2.5. MP

The MPs of three NDRAs with FCC, BCC, and HCP lattice structures — CoCrNi, MoNbTa, and HfTiZr — are calculated for both random and CSRO configurations. Other alloys are excluded from MP calculations due to the high computational expense. In addition, the MPs of individual constituent elements are obtained as references. The solid-liquid coexistence cell method [59] is used. This method adopts a cuboid and divides it into three regions: two solid (top and bottom) and a liquid region in the middle. The liquid region is initially heated to a high temperature using a constant volume and temperature (NVT) ensemble, while the solid regions are maintained at a trial MP under the NVT ensemble. Afterward, the liquid region is further cooled down to the trial MP using the NPT ensemble, and again the whole system is allowed to equilibrate under constant pressure in the NPT ensemble to check if the two phases — solid and liquid — can stably coexist. This process is carried out for an extended period, and if the solid and liquid phases are in stable contact without complete melting or solidification, the trial temperature is determined as the MP. The process is repeated with different trial temperatures to refine the result [60].

3. Results and discussion

3.1. CSRO

Fig. 1 illustrates the potential energy convergence in four NDRAs — CoCrNi, HfTiZr, MoNbTa, and NbTaV — during hybrid MD/MC simulations in the NPT ensemble. The simulations aim to form CSRO structures by allowing the system to relax at the target temperature (300 K) and zero pressure. In each plot, the potential energy decreases over time, stabilizing as the system approaches equilibrium, indicating the successful formation of CSRO. CoCrNi shows rapid convergence, while HfTiZr and NbTaV stabilize with minor fluctuations, and MoNbTa has the lowest convergence rate.

In Fig. 2, the WC parameters for 21 NDRAs are shown. Fig. 2(a) presents the WC parameter for the CSRO CoCrNi structure. Among the same-species pairs, only NiNi exhibits a positive WC value, indicating a tendency for Ni clustering. For the different-species pairs, CoCr shows a negative WC value, suggesting a likelihood of CoCr clustering

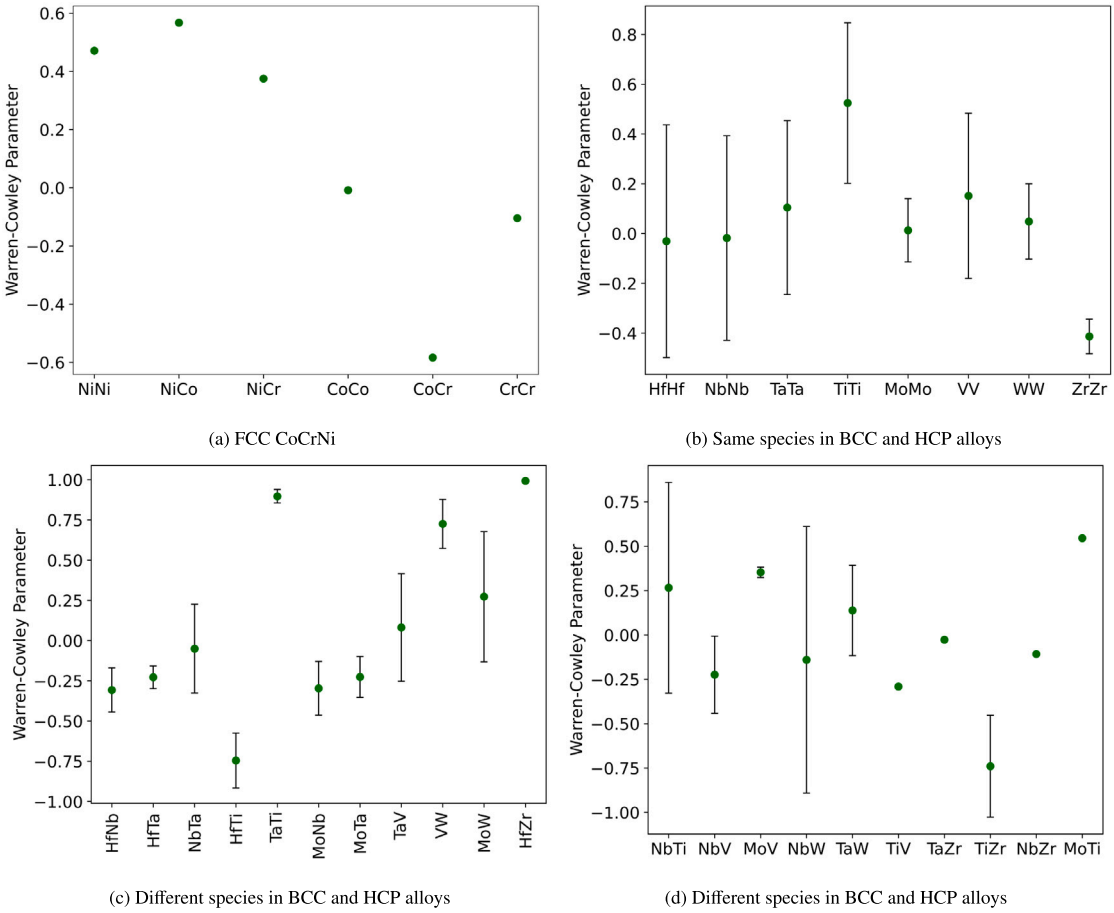

(a) FCC CoCrNi

(b) Same species in BCC and HCP alloys

(c) Different species in BCC and HCP alloys

(d) Different species in BCC and HCP alloys

Fig. 2. Pairwise WC parameters based on 21 NDRAs calculated by the EAM potential.

within the CSRO structure. From Fig. 2(b), it is observed that the WC parameter ranges for 6 out of the total 8 pairs (HfHf, NbNb, TaTa, VV, MoMo, and WW) span both positive and negative values. This suggests that these pairs do not exhibit a consistent pattern of segregation or ordering behavior across different alloys. In contrast, the TiTi pair notably shows a WC parameter range entirely in the positive region, indicating a stronger tendency for local ordering or segregation in the structure. This implies that Ti atoms in all these NDRAs tend to cluster together more frequently compared to other same-species pairs. Additionally, ZrZr pairs show a negative WC parameter. In Fig. 2(c), the WC parameters for NbTa, TaV, and MoW pairs range from negative to positive, indicating no clear pattern in their ordering behavior. Similarly, HfNb, HfTa, MoNb, and MoTa also show a range from negative to positive but with a narrower span. Notably, TaTi and VW have positive WC parameters. In contrast, HfTi exhibits a WC parameter entirely in the negative range, indicating a strong tendency for the two elements to cluster together. In Fig. 2(d), NbW, NbTi, and TaW display a wide range of WC parameters, spanning from negative to positive, reflecting inconsistent ordering behavior. TiZr, TiV, and NbZr, with minimal variation and entirely negative WC values, suggest a strong preference for ordering. All other pairs show positive WC values.

3.2. Lattice parameter

Fig. 3 compares the lattice parameters of 21 NDRAs between their CSRO structures and random counterparts. The NDRAs with larger lattice parameters in the random structure are on the left, whereas those with larger lattice parameters in the CSRO structure are on the right, as indicated by the gray dotted line. Some of the lattice parameter values for random structures were taken from existing literature [37,58,61]. In most cases, the difference in lattice parameters between random and CSRO structures is small. Out of the 21 NDRAs analyzed, 16 exhibit a larger lattice parameter in their random structures, while 5 display a larger lattice parameter in their CSRO structures. The difference is likely due to the effect of CSRO on atomic packing [32].

3.3. LD

In comparison to their CSRO counterparts, random structures typically display a larger LD, as illustrated in Fig. 4. In the FWHM approach, 18 of the NDRA's random structures exhibit greater LD; conversely, in the RMSAD method, the quantity of random alloys with higher LD is relatively smaller. Atoms are more evenly distributed in random structures. However, certain atoms group together to form a more symmetric force field in the CSRO structure, which lessens LD and atomic deviations. In the CSRO system, clustering causes substantial distortions at the interfaces of distinct atomic clusters, affecting adjacent areas. This elucidates why LD is more pronounced in certain CSRO systems compared to the random structure of the same alloy [54]. The random structures of some NDRAs, including HfTiZr, CoCrNi, NbVW, NbTiZr, NbTiV, MoNbV, HfTaTi, and HfNbTa, exhibit larger lattice parameters and LD across both FWHM and RMSAD method, compared with their CSRO counterparts. This observation aligns with findings by Han et al. [62], who reported that increased LD correlates with a larger lattice parameter in the CoNiV MPEA family.

3.4. USFE

To determine the effect of CSRO on USFE in 21 NDRAs, Fig. 5 illustrates the values of USFE in both random and CSRO structures.

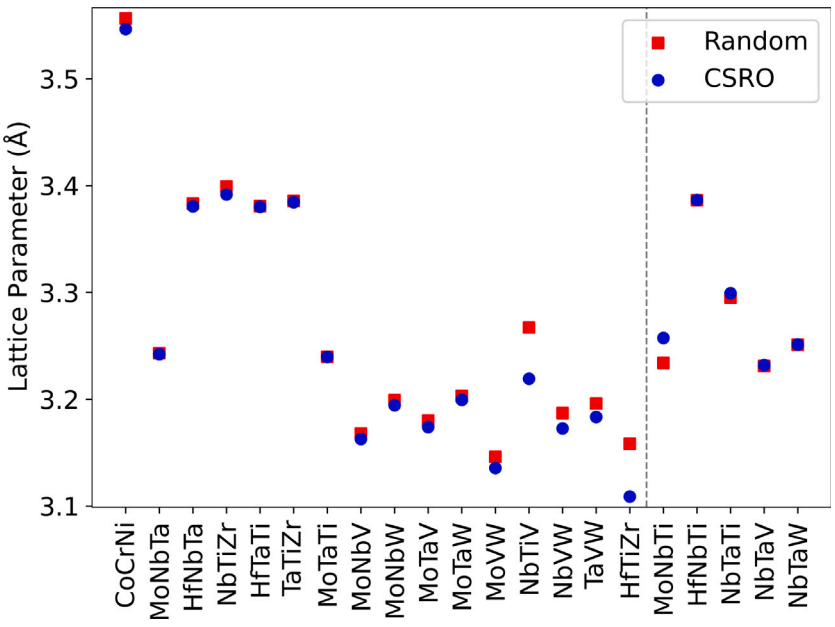

Fig. 3. Lattice parameters of 21 random and CSRO NDRAs calculated by the EAM potential. The gray dotted line separates alloys with larger lattice parameters in random structures on the left from those with larger lattice parameters in CSRO structures on the right.

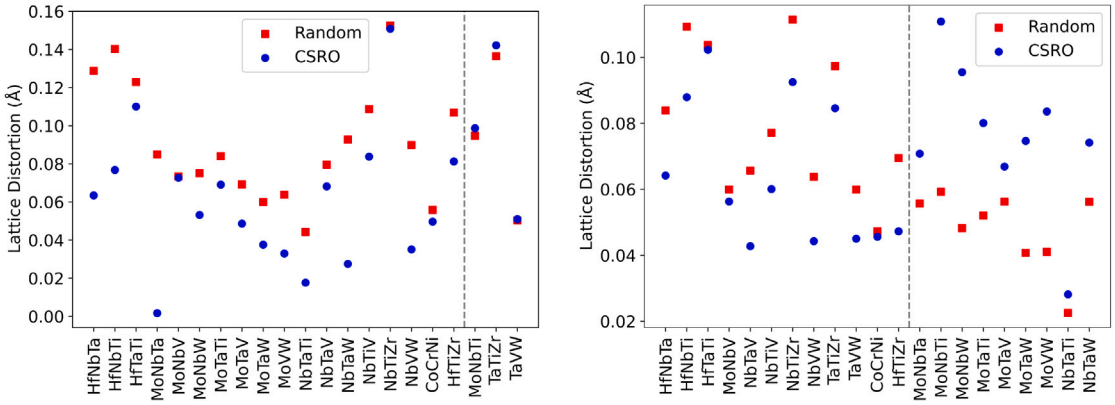

(a) FWHM (b) RMSAD

Fig. 4. LD of 21 random and CSRO NDRAs calculated by the EAM potential. Both FWHM and RMSAD methods are used. The gray dotted line separates alloys with larger LD in random structures from those with larger LD in CSRO structures.

Fig. 5(a) distinctly illustrates that a greater number of NDRAs exhibit elevated USFE within the CSRO structures. Five NDRAs i.e. NbTaW, MoNbTi, TaTiZr, MoNbV, and NbVW have not displayed a similar trend for the USFE. In Fig. 5(b), the USFE and intrinsic stacking fault energy (ISFE) values for CoCrNi and HfTiZr are shown for both random and CSRO structures. The USFE values for these CSRO alloys are higher than those of their random counterparts. The ISFE, representing the local minimum of the GSFE curve, also follows the same trend as the USFE values in both alloys. The presence of CSRO increases USFE by raising the energy barriers required for dislocations to move, thereby improving the material's resistance to deformation [37,63]. Some USFE values for the random structures were sourced from existing literature, such as MoNbTa from Mubassira et al. [37] and MoNbTi and NbTiZr from Xu et al. [58].

3.5. MP

Fig. 6 represents the trend of potential energy per atom as a function of time for the CSRO structures of MoNbTa and HfTiZr. In Fig. 6(a), the potential energy per atom of CSRO MoNbTa at temperatures below 3130 K decreases as a function of time, indicating that there is crystal growth in the solid-liquid coexistence system, resulting in solidification. On the other hand, at temperatures above 3150 K, the potential energy increases, signaling a melting transition. Therefore, the equilibrium MP for the CSRO MoNbTa structure is determined to be 3140 ± 5 K. Fig. 6(b) follows a similar pattern. To demonstrate the accuracy of our method, we compare the MPs in random and CSRO CoCrNi calculated here and those previously by Jian et al. [32]. The comparison, shown in Table B.3, is good.

Table 1 presents the MPs of CoCrNi, MoNbTa, and HfTiZr for both random and CSRO structures. The CoCrNi CSRO structure has a higher

Table 1
MP of three NDRAs in different structures, with a margin of error of ±5 K.

Alloy	Random	CSRO	Rule of mixtures
CoCrNi	1406	1430	1792.17
MoNbTa	3140	3140	3114.33
HfTiZr	1682	1715	1761.67

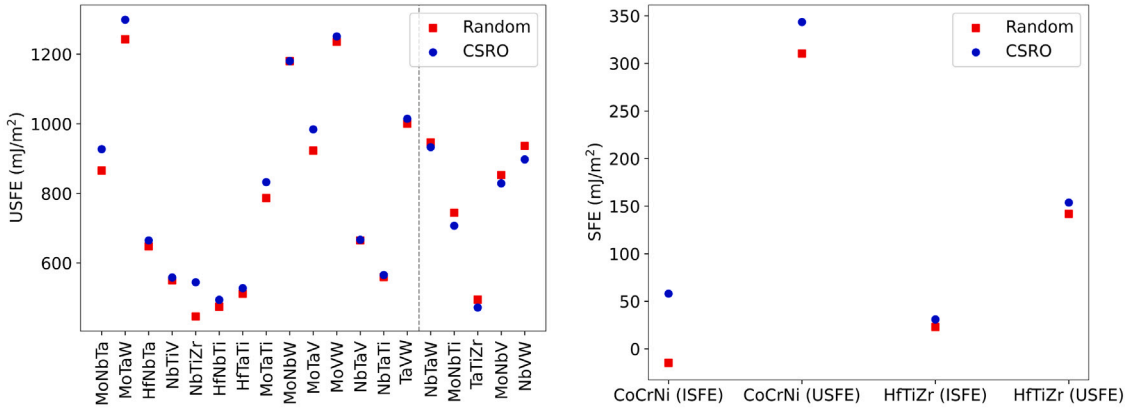

(a) USFE of 19 BCC NDRAs (b) SFE of CoCrNi and HfTiZr

Fig. 5. USFEs of 21 random and CSRO NDRAs calculated by the EAM potential. For CoCrNi and HfTiZr, ISFE values are also shown. In (a), the gray dotted line separates alloys with larger USFE in CSRO structures from those with larger USFE in random structures.

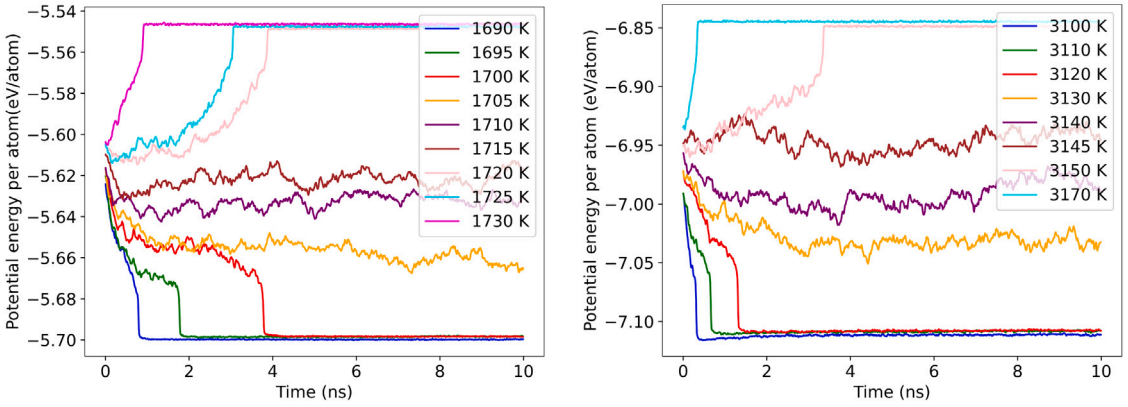

(a) MoNbTa (b) HfTiZr

Fig. 6. Evolution of the potential energy per atom of the solid–liquid coexistence cell over time at various trial temperatures for CSRO MoNbTa and CSRO HfTiZr.

Table 2
MP of pure metals with a margin of error of ±5 K.

Metal	Co	Cr	Ni	Mo	Nb	Ta	Hf	Ti	Zr
MP (K)	1732.5	1872	1772	3735	2386	3222	1945	1575	1765
	1781.5 (FCC)	1873 (FCC)	–	–	–	–	–	–	–

MP (1430 K) than the random structure (1406 K), which is expected due to the impedance of CSRO structures in the melting process. A similar trend is observed for HfTiZr, while MoNbTa shows comparable MPs between random and CSRO structures. Table 2 displays the MPs of pure metals. All metals, by default, have a lattice in their ambient conditions. For example, Cr is BCC while Co is HCP. However, the CoCrNi alloy has an FCC lattice, so we also calculate MPs of FCC Cr and FCC Co. Results show that the initial lattice type only plays a minor role in MPs. Based on the MPs of pure metals, the MPs of alloys may be estimated using the simple rule of mixtures. As shown in Table 1, for both CoCrNi and HfTiZr, the rule of mixture-based MPs are higher than both random and CSRO structures. However, MoNbTa deviates from this trend, showing a lower MP for the rule of mixture result compared to the random and CSRO structures.

3.6. Effects of the interatomic potential and the number of constituent elements

So far we have conducted an in-depth analysis of how CSRO influences selected material parameters in 21 NDRAs. All prior calculations were based on the EAM potential. Here, we extend our investigation to determine whether these findings depend on the type of interatomic potential. Specifically, we will analyze NbTaTi, NbTaV, and NbTiV using the modified embedded-atom method (MEAM) potential [64], as well as MoNbTa, MoNbV, NbTaV, and NbVW using a machine-learning-based moment tensor potential (MTP) [54]. Additionally, we will explore whether the effects of CSRO vary with the number of constituent elements in the alloy. To address this, we study three binary alloys (NbTa, NbTi, NbV), one quaternary alloy (NbTaTiV), and one quinary alloy (NbTaTiVZr) using the MEAM potential. Both potentials were validated against DFT-calculated properties, such as lattice parameters and elastic constants. Table C.4 demonstrates that the three potentials (including EAM) compare favorably with DFT in terms of USFE.

Fig. 7 displays the potential energy convergence for NbTaV during hybrid MD/MC simulations within the NPT ensemble. Fig. 7(a) and 7(b) depicts the MEAM potential and MTP respectively. In both figures, the potential energy decreases with time and stabilizes as the system approaches equilibrium, indicating the successful formation of the CSRO structure.

In Fig. 8, the WC parameters for the 8 NDRAs with the MEAM potential are presented in two categories. Fig. 8(a) shows the range of WC parameters for the same-species pairs, while Fig. 8(b) displays the WC parameter range for different-species pairs. In Fig. 8(a), pairs like NbNb, TaTa, TiTi, and VV exhibit WC parameter values ranging from negative to positive, indicating no clear pattern of local ordering

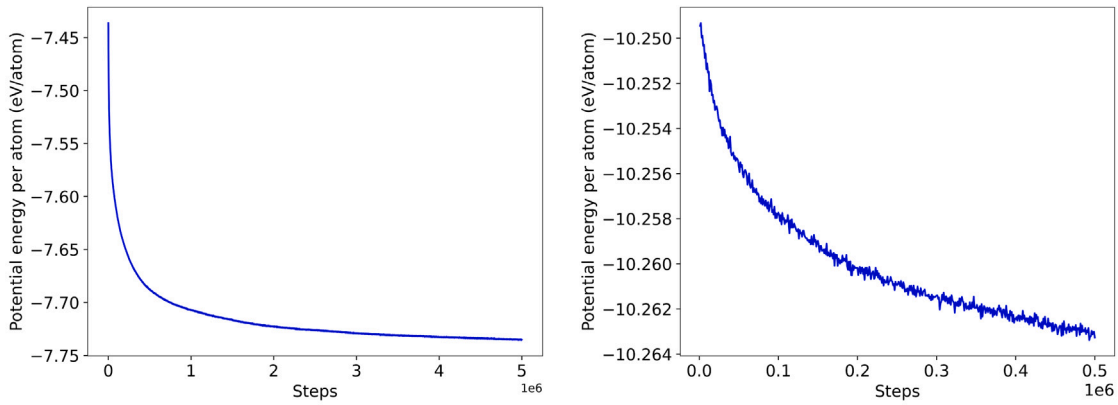

(a) MEAM (b) MTP

Fig. 7. Convergence of potential energy per atom as a function of simulation steps for the CSRO structure of NbTaV based on the (a) MEAM potential and (b) MTP.

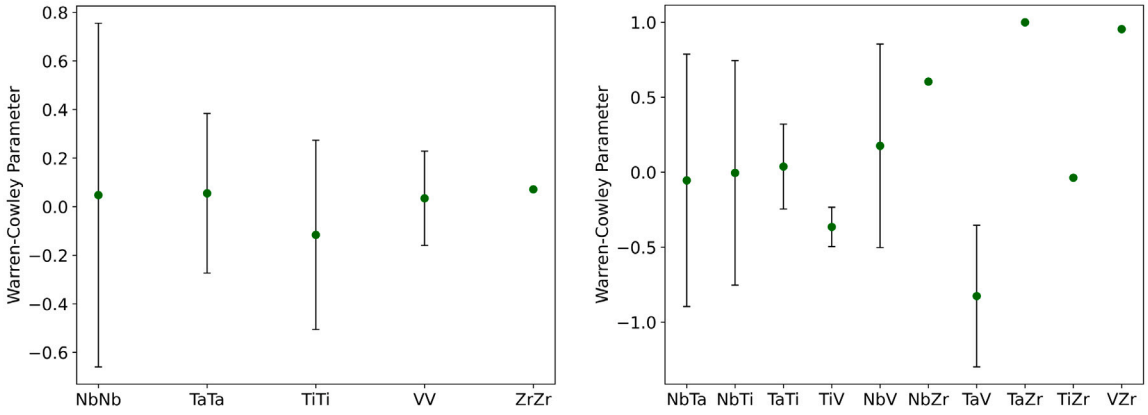

(a) Same species (b) Different species

Fig. 8. Pairwise WC parameters based on the 8 NDRAs calculated by the MEAM potential.

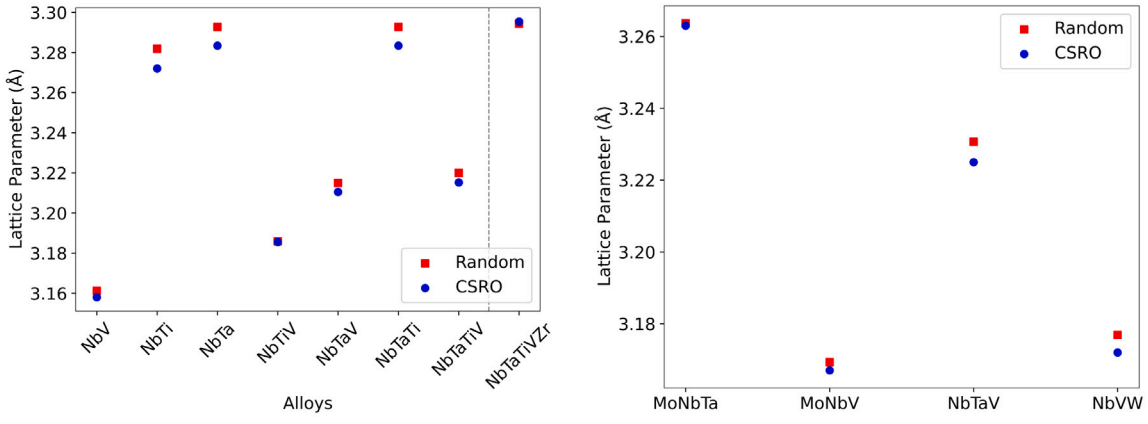

(a) MEAM (b) MTP

Fig. 9. Lattice parameters of random and CSRO NDRAs calculated by MEAM potential and MTP. In (a), the gray dotted line separates alloys with larger lattice parameters in random structures on the left from those with larger lattice parameters in CSRO structures on the right.

across all NDRAs. The ZrZr pair, however, shows a positive WC parameter of 0.072, suggesting a likelihood of clustering. In Fig. 8(b), the WC parameters for pairs like NbTa, NbTi, TaTi, and NbV also range from negative to positive, further suggesting no specific local ordering behavior. However, the TiV and TaV pairs exhibit consistently negative WC parameter ranges, from −0.233 to −0.496 and from −0.354 to −1.298, respectively, indicating a tendency for local segregation in these pairs. In contrast, pairs like NbZr, TaZr, and VZr have high positive WC parameter values.

In Fig. 9, the lattice parameters of random and CSRO NDRAs with MEAM and MTP potentials are shown. Across all binary, ternary, and quinary NDRAs, random alloys exhibit larger lattice parameters compared to their CSRO counterparts, which is the same for both MEAM potential and MTP, as well as previous findings using the EAM

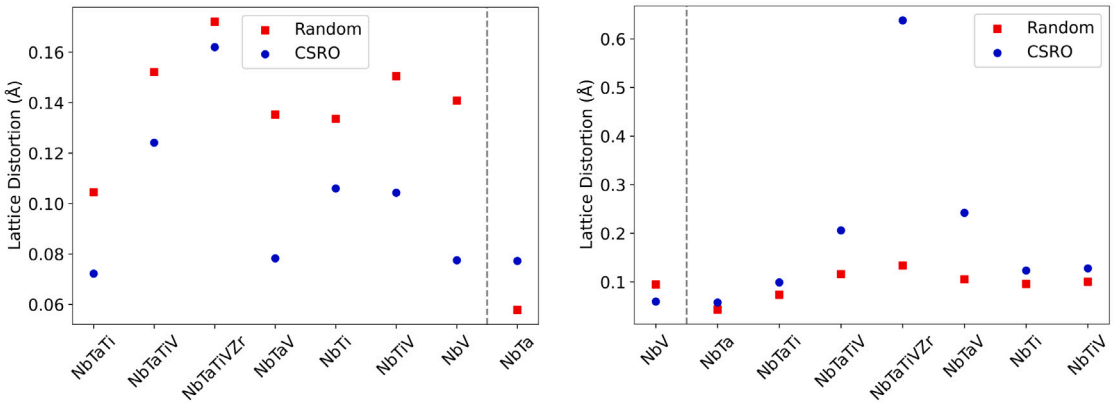

(a) FWHM (b) RMSAD

Fig. 10. LDs of random and CSRO NDRAs calculated by the MEAM potential. Both FWHM and RMSAD methods are used. The gray dotted line separates alloys with larger LD in random structures from those with larger LD in CSRO structures.

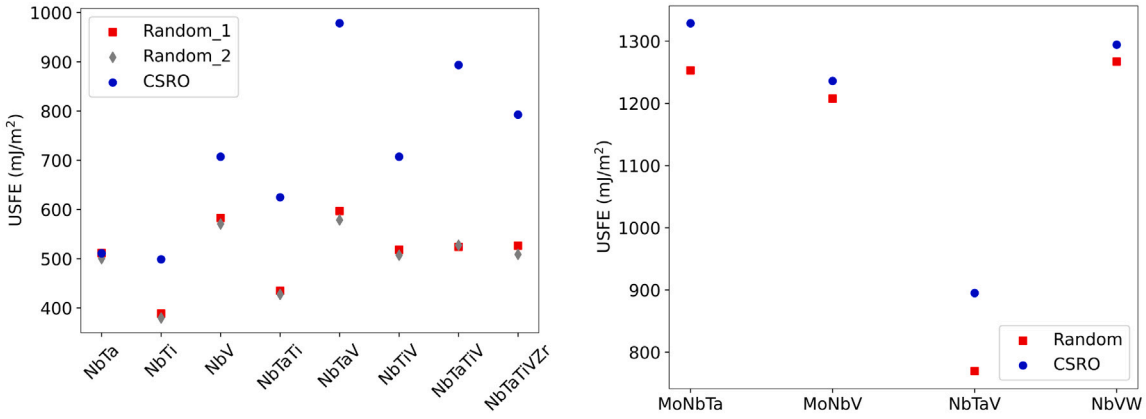

(a) MEAM (b) MTP

Fig. 11. USFEs of random and CSRO NDRAs calculated by MEAM potential and MTP.

potential. The only exception is the quaternary alloy NbTaTiZr, where the CSRO structure displays a slightly larger lattice parameter than its random counterpart.

In Fig. 10, the LD of NDRAs is calculated using the MEAM potential based on two definitions: FWHM and RMSAD, comparing both random and CSRO structures. In the FWHM method, most random NDRAs exhibit larger LD than their CSRO counterparts, with the exception of NbTa, which is consistent with results based on the EAM potential. However, the results are reversed when using the RMSAD definition, where random structures show smaller LD than CSRO structures, except for NbV. To explore this outcome, we examine the structures for the presence of the B_2 phase, which is likely to form in CSRO BCC structures [65]. We find that the B2 phase is absent in all cases except in CSRO NbTi. Hence, the difference between FWHM and RMSAD cannot be explained by the formation of B2 phases. In the meantime, a small amount of FCC phases are identified in the CSRO NbTaTiVZr CSRO, which could be contributing to the large RMSAD (but not large FWHM) observed in this alloy. This suggests that RMSAD may be a more appropriate measurement for LD because it can capture the phase transformation-induced LD.

Fig. 11 depicts USFEs of random and CSRO NDRAs using both MEAM potential and MTP. All results here point to that the CSRO USFE is higher than the random USFE for the same alloy, largely in agreement with our EAM results.

In Fig. 5, some EAM-based USFEs for the random alloys were based on relaxed structures while others were based on unrelaxed structures, although both structures had the correct lattice parameter. Hence, we are interested in exploring whether relaxation affects the USFE. In Fig. 11(a), results based on relaxed structures are referred to as Random_1, while those based on unrelaxed structures are Random_2. Only the MEAM potential is used for this purpose. It is shown that they produce very similar USFE values for the same random alloy. Hence, it is fine to ignore their difference.

4. Conclusions

In this work, we investigate the influence of CSRO on selected material properties of multiple NDRAs. CSRO structures are generated using a hybrid MD/MC approach in an NPT ensemble. Specifically, we investigate the lattice parameter, LD, USFE, and MP in both random and CSRO structures. The focus is on 21 ternary alloys using the EAM potential. Our findings show that random structures generally have larger lattice parameters and higher LD compared to the CSRO structures. The CSRO structures mostly exhibit higher USFEs and MPs, indicating that CSRO would raise the energy barriers for dislocation movement and enhance thermal stability owing to local atomic ordering. Besides, the local segregation and atomic pairing behavior change considerably across different alloys, showing no general trend but providing important insight into the complexity of the atomic interactions in these alloys.

To assess whether these results depend on the chosen interatomic potential, we perform additional analyses by using MEAM potential and MTP. Results obtained with these potentials are mostly compared well with those from the EAM potential, commenting on the robustness of

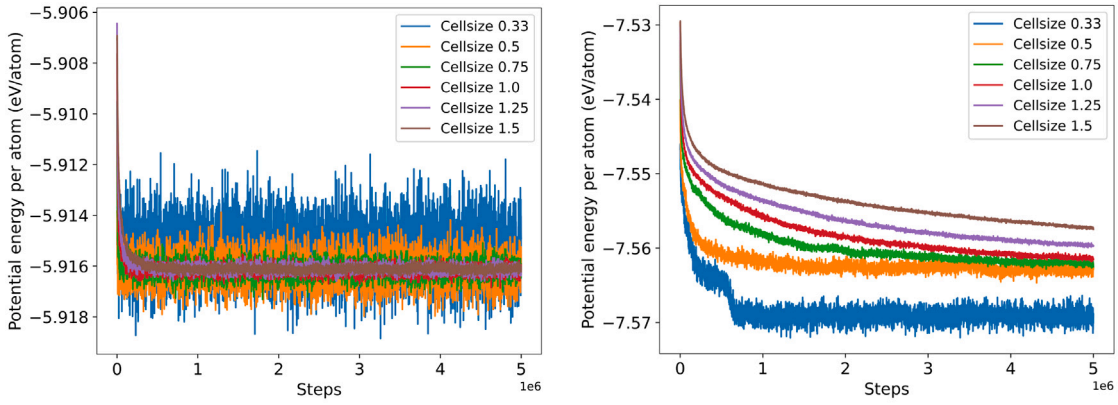

(a) HfTiZr (b) MoNbTa

Fig. A.12. Convergence of potential energy per atom as a function of simulation steps for the CSRO structures of two NDRAs: (a) HfTiZr and (b) MoNbTa, based on the EAM potential. Different cell sizes are considered.

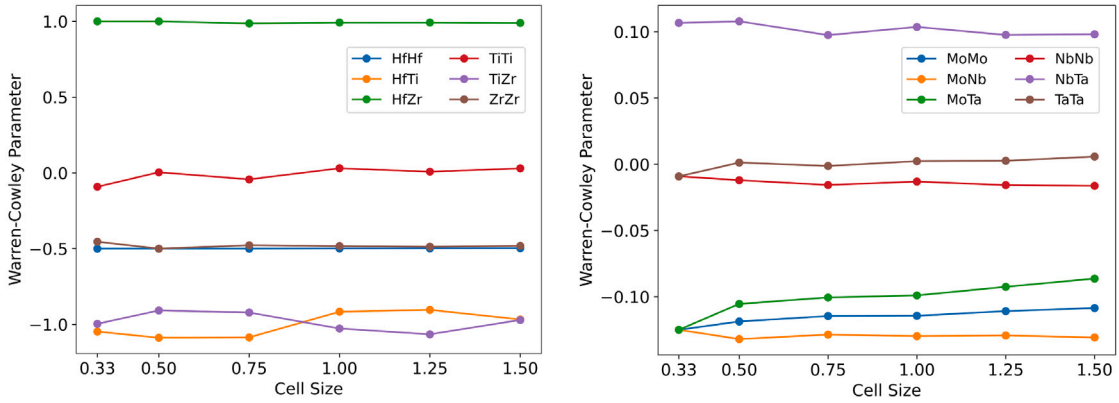

(a) HfTiZr (b) MoNbTa

Fig. A.13. Pairwise WC parameters based on two NDRAs, (a) HfTiZr and (b) MoNbTa, calculated by the EAM potential. Different cell sizes are considered.

the findings. Also, for the MEAM potential, we consider two kinds of random structures: relaxed and unrelaxed. Both yield almost the same USFE results. In summary, this work highlights the crucial role of CSRO in enhancing the mechanical and thermal properties of NDRAs. This comprehensive evaluation is critical for future design and optimization of high-performance alloys for advanced applications. This study does not address slip resistances or dislocation mobility, as they fall outside the scope of our current investigation. However, we plan to conduct a systematic study on these topics in the future, building on insights from prior research [14,54,59,63,66–69].

CRediT authorship contribution statement

Subah Mubassira: Writing – original draft, Visualization, Methodology, Investigation, Formal analysis, Data curation. **Mahshad Fani:** Investigation. **Anshu Raj:** Investigation. **Cliff Hirt:** Investigation. **Richard S. Brinlee:** Investigation. **Amin Poozesh:** Investigation. **Wu-Rong Jian:** Methodology, Investigation. **Saeed Zare Chavoshi:** Methodology. **Chanho Lee:** Methodology. **Shuozhi Xu:** Writing – review & editing, Supervision, Methodology, Funding acquisition, Conceptualization.

Declaration of competing interest

The authors declare that they have no known competing financial interests or personal relationships that could have appeared to influence the work reported in this paper.

Acknowledgments

This research was supported in part by a grant from the Research Council of the University of Oklahoma (OU) Norman Campus, United States. S.M. expresses gratitude for receiving the Dorothy Grace Barkow Scholarship awarded by OU. C.L. was supported by the Technology Innovation Program (or Industrial Strategic Technology Development Program) RS-2024-00431715 funded by the Ministry of Trade Industry & Energy (MOTIE, Korea). Additionally, S.M., M.F., A.R., and S.X. are grateful for the startup funds provided by OU, United States. This work used Bridges-2 at the Pittsburgh Supercomputing Center through allocation #MAT230058 from the Advanced Cyberinfrastructure Coordination Ecosystem: Services & Support (ACCESS) program, which is supported by National Science Foundation, United States grants #2138259, #2138286, #2138307, #2137603, and #2138296. Some of the computing for this project was performed at the OU Supercomputing Center for Education & Research (OSCER) at OU.

Appendix A. Effect of cell size on the CSRO structure generation

Here, we investigate the influence of simulation cell size on the CSRO structure generation. The EAM potnetial is used. Two alloys, namely HfTiZr and MoNbTa, are studied. Different cell sizes, with edge lengths being 0.33, 0.5, 0.75, 1, 1.25, and 1.5 times those used elsewhere in the paper, are considered. As shown in Fig. A.12, the time-dependent potential energy per atom is largely independent of the cell

Table B.3
A comparison of MP of CoCrNi between our results and literature data.

Source	Structure	MP (K)
This work	Random, no annealing	1406 ± 5
	CSRO, annealed at 300 K	1425 ± 5
	CSRO with SGC, annealed at 300 K	1430 ± 5
	CSRO with SGC, annealed at 350 K	1425 ± 5
Jian et al. [34]	Random, no annealing	1412
	CSRO with SGC, annealed at 350 K	1475

Table C.4
A comparison of USFE (in mJ/m^2) between our results and DFT data in the literature. All results are based on random alloys.

Alloy	EAM	MEAM	MTP	DFT
MoNbTa	865.43 [37]	–	1252.88	1055 [37]
MoNbV	852.74	–	1207.54	1046 [70]
NbVW	936.48	–	1267.01	1008 [70]
NbTaV	664.63	596.72	769.61	631 [70], 644 [64]
NbTaTi	559.34	435.02	–	569 [64]
NbTiV	550	517.99	–	504 [64], 491 [70]
MoNbTi	744.63 [58]	–	–	765 [58]
NbTiZr	446.54 [58]	–	–	457 [64], 390 [71]
TaTiZr	494.45	–	–	518 [64]

size. A similar pattern is observed in Fig. A.13, where pairwise WC parameters are shown, further demonstrating that the cell size chosen in the paper is good for the CSRO generation.

Appendix B. Validation of the MP calculation method

As shown in Table B.3, Jian et al. [34] used the solid-liquid coexistence method to calculate the MPs of random and CSRO CoCrNi NDRA as 1412 K and 1475 K, respectively, with the CSRO structure generated using the semi-grand canonical (SGC) method at an annealing temperature of 350 K. Using the same method, we build two CSRO structures, annealed at 300 and 350 K, respectively, and calculated their MPs as 1425 and 1430 K, respectively, which are close to the results of Jian et al. It is also shown that for the same annealing temperature of 300 K, the two CSRO structures built using the method in this work and the SGC method, respectively, possess almost identical MP.

Appendix C. Validation of the interatomic potentials in terms of USFE

In Table C.4, a comparison of USFE values calculated by the EAM potential, MEAM potential, and MTP against DFT data in the literature is displayed for various random NDRAs. Good agreement is observed, indicating the reliability and accuracy of the potentials used in this study.

Data availability

The data that support the findings of this study are openly available in three GitHub repositories https://github.com/shuozhixu/CMS-EAM_2025, https://github.com/shuozhixu/CMS-MEAM_2025, and https://github.com/shuozhixu/CMS-MTP_2025.

References

[1] Y.F. Ye, Q. Wang, J. Lu, C.T. Liu, Y. Yang, High-entropy alloy: challenges and prospects, Mater. Today 19 (2016) 349–362.

[2] A. Brezini, R. Bouamrane, F. Hamdache, C. Depolier, Theoretical model of the density of states for random dilute binary alloys, Phys. Status Solidi b 188 (1995) 697–710.

[3] S. Nag, W.A. Curtin, Effect of solute-solute interactions on strengthening of random alloys from dilute to high entropy alloys, Acta Mater. 200 (2020) 659–673.

[4] Z. Li, S. Zhao, R.O. Ritchie, M.A. Meyers, Mechanical properties of high-entropy alloys with emphasis on face-centered cubic alloys, Prog. Mater. Sci. 102 (2019) 296–345.

[5] B. Cantor, I.T.H. Chang, P. Knight, A.J.B. Vincent, Microstructural development in equiatomic multicomponent alloys, Mater. Sci. Eng. A 375–377 (2004) 213–218.

[6] J.-W. Yeh, S.-K. Chen, S.-J. Lin, J.-Y. Gan, T.-S. Chin, T.-T. Shun, C.-H. Tsau, S.-Y. Chang, Nanostructured high-entropy alloys with multiple principal elements: Novel alloy design concepts and outcomes, Adv. Eng. Mater. 6 (2004) 299–303.

[7] O.N. Senkov, G.B. Wilks, D.B. Miracle, C.P. Chuang, P.K. Liaw, Refractory high-entropy alloys, Intermetallics 18 (2010) 1758–1765.

[8] D.B. Miracle, O.N. Senkov, A critical review of high entropy alloys and related concepts, Acta Mater. 122 (2017) 448–511.

[9] Y. Zhang, T.T. Zuo, Z. Tang, M.C. Gao, K.A. Dahmen, P.K. Liaw, Z.P. Lu, Microstructures and properties of high-entropy alloys, Prog. Mater. Sci. 61 (2014) 1–93.

[10] Q.-J. Li, H. Sheng, E. Ma, Strengthening in multi-principal element alloys with local-chemical-order roughened dislocation pathways, Nature Commun. 10 (2019) 3563.

[11] R. Gröger, V. Vitek, A. Dlouhý, Effective pair potential for random fcc CoCrFeMnNi alloys, Modelling Simul. Mater. Sci. Eng. 28 (2020) 075006.

[12] W. Li, S.I. Rao, Q. Wang, H. Fan, J. Yang, J.A. El-Awady, Core structure and mobility of edge dislocations in face-centered-cubic chemically complex NiCoFe and NiCoFeCu equiatomic solid-solution alloys, Materialia 9 (2020) 100628.

[13] S.I. Rao, C. Woodward, T.A. Parthasarathy, O. Senkov, Atomistic simulations of dislocation behavior in a model FCC multicomponent concentrated solid solution alloy, Acta Mater. 134 (2017) 188–194.

[14] E. Antillon, C. Woodward, S.I. Rao, B. Akdim, T.A. Parthasarathy, Chemical short range order strengthening in a model FCC high entropy alloy, Acta Mater. 190 (2020) 29–42.

[15] R. Pasianot, D. Farkas, Atomistic modeling of dislocations in a random quinary high-entropy alloy, Comput. Mater. Sci. 173 (2020) 109366.

[16] O.N. Senkov, D.B. Miracle, K.J. Chaput, J.-P. Couzinie, Development and exploration of refractory high entropy alloys—a review, J. Mater. Res. 33 (2018) 3092–3128.

[17] J.P. Couzinié, G. Dirras, Body-centered cubic high-entropy alloys: From processing to underlying deformation mechanisms, Mater. Charact. 147 (2019) 533–544.

[18] O.N. Senkov, S. Gorsse, D.B. Miracle, High temperature strength of refractory complex concentrated alloys, Acta Mater. 175 (2019) 394–405.

[19] O.N. Senkov, S.I. Rao, T.M. Butler, K.J. Chaput, Ductile nb alloys with reduced density and cost, J. Alloys Compd. 808 (2019) 151685.

[20] O.N. Senkov, S. Rao, K.J. Chaput, C. Woodward, Compositional effect on microstructure and properties of NbTiZr-based complex concentrated alloys, Acta Mater. 151 (2018) 201–215.

[21] J.B. Lambert, Refractory metals and alloys, in: ASM Handbook Volume 2: Properties and Selection: Nonferrous Alloys and Special-Purpose Materials, ASM International, 1990, pp. 557–585, URL https://dl.asminternational.org/h{andb}ooks/edited-volume/14/chapter/201131/Refractory-Metals-and-Alloys.

[22] R. Zhang, S. Zhao, J. Ding, Y. Chong, T. Jia, C. Ophus, M. Asta, R.O. Ritchie, A.M. Minor, Short-range order and its impact on the CrCoNi medium-entropy alloy, Nature 581 (2020) 283–287.

[23] X. Chen, Q. Wang, Z. Cheng, M. Zhu, H. Zhou, P. Jiang, L. Zhou, Q. Xue, F. Yuan, J. Zhu, X. Wu, E. Ma, Direct observation of chemical short-range order in a medium-entropy alloy, Nature 592 (2021) 712–716.

[24] D.L. Foley, A.K. Barnett, Y. Rakita, A. Perez, P.P. Das, S. Nicolopoulos, D.E. Spearot, I.J. Beyerlein, M.L. Falk, M.L. Taheri, Diffuse electron scattering reveals kinetic frustration as origin of order in CoCrNi medium entropy alloy, Acta Mater. 268 (2024) 119753.

[25] F. Zhang, S. Zhao, K. Jin, H. Xue, G. Velisa, H. Bei, R. Huang, J. Ko, D. Pagan, J. Neuefeind, W. Weber, Y. Zhang, Local structure and short-range order in a NiCoCr solid solution alloy, Phys. Rev. Lett. 118 (2017) 205501.

[26] J. Ding, Q. Yu, M. Asta, R.O. Ritchie, Tunable stacking fault energies by tailoring local chemical order in CrCoNi medium-entropy alloys, Proc. Natl. Acad. Sci. 115 (2018) 8919–8924.

[27] S.D. Wang, X.J. Liu, Z.F. Lei, D.Y. Lin, F.G. Bian, C.M. Yang, M.Y. Jiao, Q. Du, H. Wang, Y. Wu, S.H. Jiang, Z.P. Lu, Chemical short-range ordering and its strengthening effect in refractory high-entropy alloys, Phys. Rev. B 103 (2021) 104107.

[28] P. Singh, A.V. Smirnov, D.D. Johnson, Atomic short-range order and incipient long-range order in high-entropy alloys, Phys. Rev. B 91 (2015) 224204.

[29] J.S. Wróbel, D. Nguyen-Manh, M.Y. Lavrentiev, M. Muzyk, S.L. Dudarev, Phase stability of ternary fcc and BCC Fe-Cr-Ni alloys, Phys. Rev. B 91 (2015) 024108.

[30] A. Fernández-Caballero, J.S. Wróbel, P.M. Mummery, D. Nguyen-Manh, Short-range order in high entropy alloys: Theoretical formulation and application to Mo-Nb-Ta-V-W system, J. Phase Equilib. Diffus. 38 (2017) 391–403.

[31] Y. Ma, Q. Wang, C. Li, L.J. Santodonato, M. Feygenson, C. Dong, P.K. Liaw, Chemical short-range orders and the induced structural transition in high-entropy alloys, Scr. Mater. 144 (2018) 64–68.

[32] W.-R. Jian, Z. Xie, S. Xu, Y. Su, X. Yao, I.J. Beyerlein, Effects of lattice distortion and chemical short-range order on the mechanisms of deformation in medium entropy alloy CoCrNi, Acta Mater. 199 (2020) 352–369.
[33] S. Zhao, Local ordering tendency in body-centered cubic (BCC) multi-principal element alloys, J. Phase Equilib. Diffus. 42 (2021) 578–591.
[34] W.-R. Jian, L. Wang, W. Bi, S. Xu, I.J. Beyerlein, Role of local chemical fluctuations in the melting of medium entropy alloy CoCrNi, Appl. Phys. Lett. 119 (2021) 121904.
[35] Z. Xie, W.-R. Jian, S. Xu, I.J. Beyerlein, X. Zhang, Z. Wang, X. Yao, Role of local chemical fluctuations in the shock dynamics of medium entropy alloy CoCrNi, Acta Mater. 221 (2021) 117380.
[36] S. Yin, J. Ding, M. Asta, R.O. Ritchie, Ab initio modeling of the energy landscape for screw dislocations in body-centered cubic high-entropy alloys, npj Comput. Mater. 6 (2020) 110.
[37] S. Mubassira, W.-R. Jian, S. Xu, Effects of chemical short-range order and temperature on basic structure parameters and stacking fault energies in multi-principal element alloys, Modelling 5 (2024) 352–366.
[38] A.P. Thompson, H.M. Aktulga, R. Berger, D.S. Bolintineanu, W.M. Brown, P.S. Crozier, P.J. in 't Veld, A. Kohlmeyer, S.G. Moore, T.D. Nguyen, R. Shan, M.J. Stevens, J. Tranchida, C. Trott, S.J. Plimpton, LAMMPS - a flexible simulation tool for particle-based materials modeling at the atomic, meso, and continuum scales, Comput. Phys. Comm. 271 (2022) 108171.
[39] M.S. Daw, M.I. Baskes, Embedded-atom method: Derivation and application to impurities, surfaces, and other defects in metals, Phys. Rev. B 29 (1984) 6443–6453.
[40] S.I. Rao, C. Woodward, B. Akdim, O.N. Senkov, D. Miracle, Theory of solid solution strengthening of BCC chemically complex alloys, Acta Mater. 209 (2021) 116758.
[41] X.W. Zhou, R.A. Johnson, H.N.G. Wadley, Misfit-energy-increasing dislocations in vapor-deposited CoFe/NiFe multilayers, Phys. Rev. B 69 (2004) 144113.
[42] D.-Y. Lin, S.S. Wang, D.L. Peng, M. Li, X.D. Hui, An n-body potential for a Zr–Nb system based on the embedded-atom method, J. Phys.: Condens. Matter. 25 (2013) 105404.
[43] A. Ghafarollahi, F. Maresca, W.A. Curtin, Solute/screw dislocation interaction energy parameter for strengthening in BCC dilute to high entropy alloys, Modell. Simul. Mater. Sci. Eng. 27 (2019) 085011.
[44] H. Zheng, L.T.W. Fey, X.-G. Li, Y.-J. Hu, L. Qi, C. Chen, S. Xu, I.J. Beyerlein, S.P. Ong, Multi-scale investigation of short-range order and dislocation glide in MoNbTi and TaNbTi multi-principal element alloys, npj Comput. Mater. 9 (2023) 89.
[45] X. Huang, L. Liu, X. Duan, W. Liao, J. Huang, H. Sun, C. Yu, Atomistic simulation of chemical short-range order in HfNbTaZr high entropy alloy based on a newly-developed interatomic potential, Mater. Des. 202 (2021) 109560.
[46] S. Chen, Z.H. Aitken, S. Pattamatta, Z. Wu, Z.G. Yu, D.J. Srolovitz, P.K. Liaw, Y.-W. Zhang, Simultaneously enhancing the ultimate strength and ductility of high-entropy alloys via short-range ordering, Nature Commun. 12 (2021) 4953.
[47] J.M. Cowley, An approximate theory of order in alloys, Phys. Rev. 77 (1950) 669–675.
[48] D. de Fontaine, The number of independent pair-correlation functions in multicomponent systems, J. Appl. Crystallogr. 4 (1971) 15–19.
[49] H. Ge, F. Tian, A review of ab initio calculation on lattice distortion in high-entropy alloys, JOM 71 (2019) 4225–4237.
[50] Y. Zhang, Y.J. Zhou, J.P. Lin, G.L. Chen, P.K. Liaw, Solid-solution phase formation rules for multi-component alloys, Adv. Eng. Mater. 10 (2008) 534–538.
[51] L.R. Owen, N.G. Jones, Quantifying local lattice distortions in alloys, Scr. Mater. 187 (2020) 428–433.
[52] H. Song, F. Tian, Q.-M. Hu, L. Vitos, Y. Wang, J. Shen, N. Chen, Local lattice distortion in high-entropy alloys, Phys. Rev. Mater. 1 (2017) 023404.
[53] N.L. Okamoto, K. Yuge, K. Tanaka, H. Inui, E.P. George, Atomic displacement in the CrMnFeCoNi high-entropy alloy – a scaling factor to predict solid solution strengthening, AIP Adv. 6 (2016) 125008.
[54] T. Wang, J. Li, M. Wang, C. Li, Y. Su, S. Xu, X.-G. Li, Unraveling dislocation-based strengthening in refractory multi-principal element alloys, npj Comput. Mater. 10 (2024) 143.
[55] Y. Su, S. Xu, I.J. Beyerlein, Ab initio-informed phase-field modeling of dislocation core structures in equal-molar CoNiRu multi-principal element alloys, Modelling Simul. Mater. Sci. Eng. 27 (2019) 084001.
[56] M. Beyramali Kivy, M. Asle Zaeem, Generalized stacking fault energies, ductilities, and twinnabilities of CoCrFeNi-based face-centered cubic high entropy alloys, Scr. Mater. 139 (2017) 83–86.
[57] S. Zhao, Y. Osetsky, G.M. Stocks, Y. Zhang, Local-environment dependence of stacking fault energies in concentrated solid-solution alloys, npj Comput. Mater. 5 (2019) 13.
[58] S. Xu, E. Hwang, W.-R. Jian, Y. Su, I.J. Beyerlein, Atomistic calculations of the generalized stacking fault energies in two refractory multi-principal element alloys, Intermetallics 124 (2020) 106844.
[59] S. Mishra, K. Guda Vishnu, A. Strachan, Comparing the accuracy of melting temperature prediction methods for high entropy alloys, J. Appl. Phys. 132 (2022) 205901.
[60] S.Z. Chavoshi, S. Xu, S. Goel, Addressing the discrepancy of finding the equilibrium melting point of silicon using molecular dynamics simulations, Proc. R. Soc. A: Math. Phys. Eng. Sci. 473 (2017) 20170084.
[61] S. Xu, S.Z. Chavoshi, Y. Su, On calculations of basic structural parameters in multi-principal element alloys using small atomistic models, Comput. Mater. Sci. 202 (2022) 110942.
[62] Z. Han, S. Peng, H. Feng, Y. Chen, J. Li, Q. Fang, Lattice distortion dependent physical and mechanical properties of VCoNi multi-principal element alloys, J. Alloys Compd. 1005 (2024) 175421.
[63] S. Lyu, W. Li, Y. Xia, Y. Chen, A.H.W. Ngan, Effects of chemical randomness on strength contributors and dislocation behaviors in a bcc multiprincipal element alloy, Phys. Rev. Mater. 7 (2023) 073602.
[64] M.S. Nitol, M.J. Echeverria, K. Dang, M.I. Baskes, S.J. Fensin, New modified embedded-atom method interatomic potential to understand deformation behavior in VNbTaTiZr refractory high entropy alloy, Comput. Mater. Sci. 237 (2024) 112886.
[65] Y. Yao, J. Cappola, Z. Zhang, Q. Zhu, W. Cai, X. Yu, L. Li, Nanostructure and dislocation interactions in refractory complex concentrated alloy: From chemical short-range order to nanoscale B2 precipitates, Acta Mater. 281 (2024) 120457.
[66] B. Chen, S. Li, J. Ding, X. Ding, J. Sun, E. Ma, Trade-off between local chemical order and lattice distortion in affecting dislocation motion in NbTiZr multi-principal element alloys, Acta Mater. 272 (2024) 119910.
[67] S. Yin, Y. Zuo, A. Abu-Odeh, H. Zheng, X.-G. Li, J. Ding, S.P. Ong, M. Asta, R.O. Ritchie, Atomistic simulations of dislocation mobility in refractory high-entropy alloys and the effect of chemical short-range order, Nature Commun. 12 (2021) 4873.
[68] L. Zhao, H. Zong, X. Ding, T. Lookman, Anomalous dislocation core structure in shock compressed bcc high-entropy alloys, Acta Mater. 209 (2021) 116801.
[69] X. Liu, W.A. Curtin, Atomistic simulations reveal strength reductions due to short-range order in alloys, Acta Mater. 263 (2024) 119471.
[70] S.M. Shaikh, B.S. Murty, S.K. Yadav, On the influence of enthalpy of formation on lattice distortion and intrinsic ductility of concentrated refractory alloys, J. Appl. Phys. 134 (2023) 035102.
[71] B. Akdim, C. Woodward, S. Rao, E. Antillon, Predicting core structure variations and spontaneous partial kink formation for $\frac{1}{2}\langle 111\rangle$ screw dislocations in three BCC NbTiZr alloys, Scr. Mater. 199 (2021) 113834.